ELSEVIER

Thin shell and surface crack finite elements for simulation of combined failure modes

B. Skallerud [a,*], K. Holthe [a], B. Haugen [b]

[a] *Department of Structural Engineering, The Norwegian University of Science and Technology, N-7491, Trondheim, Norway*
[b] *FEDEM Technology a.s., Boulder, USA*

This paper is dedicated to Professor K. Bell on the occasion of his 65th anniversary

Abstract

In this study we present a new approach to analyse cracked shell structures subjected to large geometric changes. It is based on a combination of a rectangular assumed natural deviatoric strain thin shell finite element and an improved linespring finite element. Plasticity is accounted for using stress resultants. A power law hardening model is used for shell and linespring material. A co-rotational formulation is employed to represent nonlinear geometry effects. With this, one can carry out nonlinear fracture mechanics assessments in structures that show instabilities due buckling (local/global), ovalisation and large rigid body motion. By numerical examples it is shown how geometric instabilities and fracture compete as governing failure mode.
© 2005 Elsevier B.V. All rights reserved.

1. Introduction

Surface cracked shell structures occur in many industrial applications, e.g. pressure vessels, pipelines, tubular frame structures. Two main facts cause the occurrence of defects: the shell segments that the structure are fabricated from are usually joined with welds, and most structures are subjected some cyclic loading that promote fatigue crack growth. Although welding procedures have improved significantly over the

---
* Corresponding author. Tel.: +47 73 59 35 60; fax: +47 73 59 34 91.
E-mail addresses: bjorn.skallerud@ntnu.no, bjorn.skallerud@mtf.ntnu.no (B. Skallerud).

years, some initial defects have to be expected and accounted for. In some applications the structure is subjected to very high loads. Traditional design rules for defect assessment often state that no defect can be accepted at all under loading conditions causing significant inelasticity. Hence, more advanced numerical assessment is the only way out of this dilemma. Traditionally, three-dimensional solid finite elements are employed in discretising the shell structure in order to account for the crack. Fig. 1 illustrates a typical mesh. This puts high demands on both pre- and post-processing in addition to long cpu times. An alternative is to use shell finite elements. Then the challenge is to account for the crack. This may be done using line spring finite elements at the crack location. Fig. 1 also illustrate such a mesh. For the meshes shown, a typical solid finite element mesh will have some 30,000 degrees of freedom (utilising two symmetry planes), whereas the shell model will have some 1000 DOF (using symmetry). A factor of 10 in reduced cpu is typical. But the main benefit of using shell/linespring elements is the reduced time spent in pre- and post-processing. Using linesprings, the crack is modelled as nonlinear springs between the shell elements, with a varying compliance as a function of crack depth and plastic deformations. The accuracy of the predicted fracture mechanics quantities such as crack tip opening displacement (CTOD) and *J*-integral is crucial for such an approach. The linespring element has a long history [1–4], and is implemented in some commercial codes. However, some limitations still exist, e.g. how to treat short cracks and large deformations. Short cracks are the most relevant in practical situations, that is cracks of depths less than about 25% of the shell thickness. In many applications there also is a need to account for large displacements and rotations, and simultaneously assess the criticality of the defect. In the present study these aspects are accounted for and implemented in a new commercial code denoted LINK. It is a general nonlinear shell finite element program accounting for large rigid body motion and plasticity. The shell element is a rectangular ANDES element in a co-rotated formulation [5,6]. The local strains are assumed small. Within this formulation an improved linespring finite element is implemented. Some background of the present linespring formulation is given in [7]. With this, one has a tool that can account for cracks and global/local buckling in the same simulation. One important industrial case where this is relevant is in laying of pipelines by means of reeling, with nominal strains that reach about 2% (both in tension and compression).
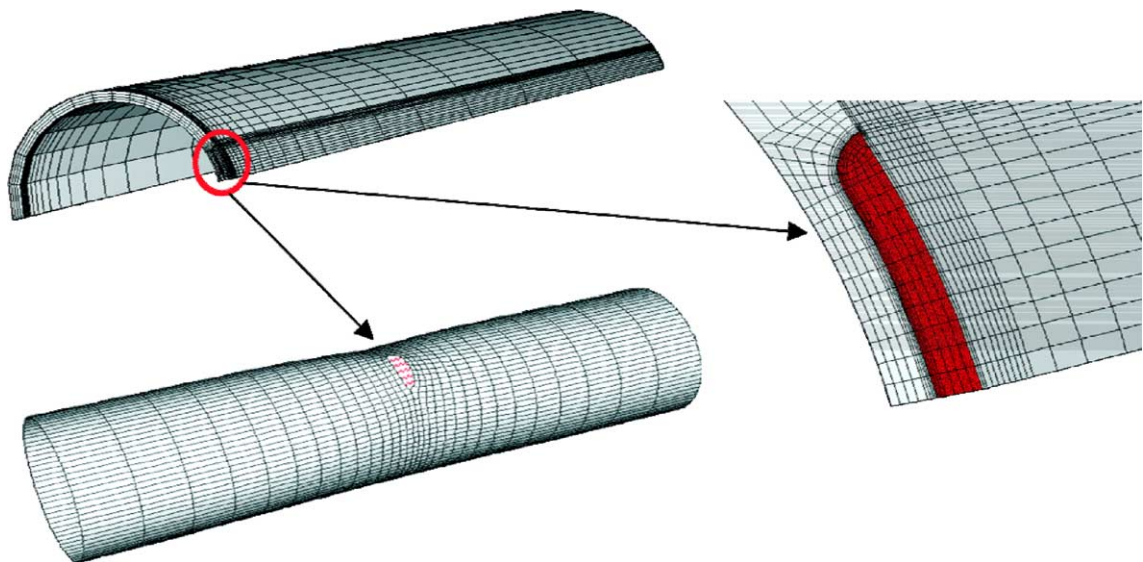

Fig. 1. Solid and shell/linespring modelling of surface cracked shells.

The first part of the paper addresses the basic shell finite element formulation, followed by the linespring formulation. Finally, some numerical test cases are presented. Here the shell/linespring simulation results are compared with detailed solid finite element results obtained using ABAQUS [8].

2. Shell finite element

The derivations for the co-rotated ANDES finite element are rather lengthy and involved. A detailed account is provided in [5,9]. In the following the basic relationships are presented. A difference in the present study compared to e.g. [5] is that a quadri-lateral ANDES finite element is employed, in [5] a triangular facet element was used. The 4-node ANDES shell element is developed as a flat element with decoupled membrane and bending behavior. The element stiffness for the ANDES element is the sum of the basic and higher order stiffness contributions

$$\mathbf{K} = \mathbf{K}_b + \mathbf{K}_h = \frac{1}{A}\mathbf{L}\mathbf{C}\mathbf{L}^T + \int_A \mathbf{B}^T\mathbf{C}\mathbf{B}\,\mathrm{d}A. \tag{1}$$

2.1. The membrane element

Nygård [23] developed a 4-node membrane element with drilling degrees of freedom based on the Free Formulation, called the FFQ element. The element gives accurate results for plane membrane problems, but is computationally expensive due to a numerical inversion of a 12×12 matrix. The present element was developed based on the ANDES formulation in order to avoid the expensive matrix inversion.

2.1.1. Membrane basic stiffness
A very successful lumping scheme for membrane stresses was first introduced by Bergan and Felippa [22], and since used by Nygård [23] and Militello [24]. With a nodal DOF ordering for $\mathbf{v}_{mi} = [u\ v\ \theta_z]$ the lumping matrix can be written as

$$\mathbf{L} = \begin{bmatrix} \mathbf{L}_1 \\ \mathbf{L}_2 \\ \mathbf{L}_3 \\ \mathbf{L}_4 \end{bmatrix}, \quad \text{where } \mathbf{L}_j = \frac{1}{2}\begin{bmatrix} y_{ki} & 0 & -x_{ki} \\ 0 & -x_{ki} & y_{ki} \\ \frac{\alpha}{6}(y_{ij}^2 - y_{kj}^2) & \frac{\alpha}{6}(x_{ij}^2 - x_{kj}^2) & \frac{\alpha}{3}(x_{kj}y_{kj} - x_{ij}y_{ij}) \end{bmatrix}. \tag{2}$$

The nodal indices (i,j,k,l) undergo cyclic permutations of $(1,2,3,4)$ in the equation above. One has also used the notation $x_{ij} = x_i - x_j$. Factor α represents a scaling of the contributions of the drilling freedom to the normal boundary displacements, see [22] for details.

2.1.2. Membrane higher order stiffness
The distribution of higher order strain is expressed in terms of natural strain gage readings as function of the higher order degrees of freedom

$$\tilde{\mathbf{v}}^T = \begin{bmatrix} \theta_1' & \theta_2' & \theta_3' & \theta_4' & \bar{\theta} & \alpha_1 & \alpha_2 \end{bmatrix}, \tag{3}$$

where θ_i' are deviatoric nodal rotations, $\bar{\theta}$ is mean nodal rotation, and α_1 and α_2 are higher order modes described by the translational degrees of freedom.

Strain gages are located at the nodes, in the two median direction (ξ and η) as well as the direction of the diagonal through the neighboring nodes (Fig. 2). For node 1 the template for the strain gage readings is
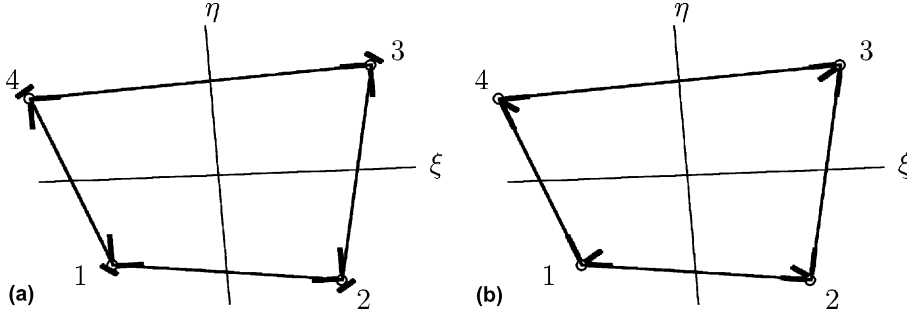
Fig. 2. Nodal strain gages: (a) membrane strain gages and (b) bending curvature gages.

$$\mathbf{Q}_1 = \begin{bmatrix} \rho_1 \chi_{\xi|1} & \rho_2 \chi_{\xi|1} & \rho_3 \chi_{\xi|1} & \rho_4 \chi_{\xi|1} & \alpha \chi_{\xi t} & -\beta_1 \dfrac{\chi_{\xi|1}}{\bar{\chi}_\xi l_\xi} & 0 \\[2ex] -\rho_1 \chi_{\eta|1} & -\rho_4 \chi_{\eta|1} & -\rho_3 \chi_{\eta|1} & -\rho_2 \chi_{\eta|1} & -\alpha \chi_{\eta t} & 0 & -\beta_1 \dfrac{\chi_{\eta|1}}{\bar{\chi}_\eta l_\eta} \\[2ex] \rho_5 \chi_{24} & \rho_6 \chi_{24} & \rho_7 \chi_{24} & \rho_8 \chi_{24} & 0 & \beta_2 \dfrac{c_{24\xi}}{l_{24}} & -\beta_2 \dfrac{c_{24\xi}}{l_{24}} \end{bmatrix}, \tag{4}$$

where $c_{13\xi} = \mathbf{s}_{13}^{\mathrm{T}} \mathbf{s}_\xi$, $c_{13\eta} = \mathbf{s}_{13}^{\mathrm{T}} \mathbf{s}_\eta$, $c_{24\xi} = \mathbf{s}_{24}^{\mathrm{T}} \mathbf{s}_\xi$ and $c_{24\eta} = \mathbf{s}_{24}^{\mathrm{T}} \mathbf{s}_\eta$. $\chi_{\xi|i} = \frac{d_{\xi|i}}{l_\xi}$ and $\chi_{\eta|i} = \frac{d_{\eta|i}}{l_\eta}$ where $d_{\xi|i}$ and $d_{\eta|i}$ are distances from node i to median lines ξ and η. l_ξ and l_η are lenghts of median lines ξ and η. $\bar{\chi}_\xi = \frac{1}{4} \sum_{i=1}^{4} \chi_{\xi|i}$ and $\bar{\chi}_\eta = \frac{1}{4} \sum_{i=1}^{4} \chi_{\eta|i}$. E.g. $\mathbf{s}_{13}$ is the unit direction vector along side 13, $\mathbf{s}_\xi$ is unit vector in ξ-direction, etc. $\mathbf{Q}_2$, $\mathbf{Q}_3$ and $\mathbf{Q}_4$ can be established by permutations of the expression above. The Cartesian strain displacement relationship at each node is established by transformation of the strain gage strains. Based on symbolic evaluation of pure bending of the element one has chosen the following set of parameters: $\rho_1 = 0.1$, $\rho_2 = -0.1$, $\rho_3 = -0.1$, $\rho_4 = 0.1$, $\rho_5 = 0$, $\rho_6 = 0.5$, $\rho_7 = 0$, $\rho_8 = -0.5$, $\beta_1 = 0.6$, $\beta_2 = 0$.

2.2. The bending element

The present element is a Kirchoff type plate element utilizing reference lines to model the plate bending behavior. Hrennikoff [25] first used this concept for modeling bending of flat plates. Park and Stanley [26] used this concept for developing several plate and shell elements based on the assumed natural-coordinate strains formulation, ANS.

2.2.1. Bending basic stiffness
The basic stiffness for the quadrilateral bending element has been developed by extending the triangle element lumping matrices of Militello to four nodes. Militello developed expressions for both linear and quadratic normal rotation. Expression given here use the quadratic normal rotation interpolation. With a nodal DOF ordering for $\mathbf{v}_{bi} = [w \; \theta_x \; \theta_y]$ the lumping matrix can be written as

$$\mathbf{L} = \begin{bmatrix} \mathbf{L}_1 \\ \mathbf{L}_2 \\ \mathbf{L}_3 \\ \mathbf{L}_4 \end{bmatrix}, \tag{5}$$

where

$$\mathbf{L}_j = \frac{1}{2} \begin{bmatrix} -c_{jk}s_{jk} + c_{ij}s_{ij} & c_{jk}s_{jk} - c_{ij}s_{ij} & -(s_{jk}^2 - c_{jk}^2) + (s_{ij}^2 + s_{ij}^2) \\ \frac{\alpha}{2}(s_{jk}^2 x_{jk} - s_{ij}^2 x_{ij}) & \frac{\alpha}{2}(c_{jk}^2 x_{jk} - c_{ij}^2 x_{ij}) & -s_{jk}^2 y_{jk} - s_{ij}^2 y_{ij} \\ \frac{\alpha}{2}(s_{jk}^2 y_{jk} - s_{ij}^2 y_{ij}) & \frac{\alpha}{2}(c_{jk}^2 y_{jk} - c_{ij}^2 y_{ij}) & -s_{jk}^2 x_{jk} - s_{ij}^2 x_{ij} \end{bmatrix}. \tag{6}$$

The nodal indices (i, j, k, l) undergo cyclic permutations of $(1, 2, 3, 4)$ in the equation above. One has also used the notation $x_{ij} = x_i - x_j$. c_{ij} and s_{ij} are cosine and sine of side ij angle with respect to x-axis, etc. Factor α represents a scaling of the contributions of the drilling freedom to the normal boundary displacements, see [22] for details.

2.2.2. Bending higher order stiffness

The higher order bending stiffness is computed as the deviatoric part of an ANS type element with nodal strain gages along element reference lines. The reference lines are the element edges and diagonals, giving a total of 12 curvature gages.

The nodal curvature of a Euler–Bernoulli beam from node i to j can be shown to be

$$\begin{bmatrix} \kappa_{ij|i} \\ \kappa_{ij|j} \end{bmatrix} = \frac{1}{l_{ij}^2} \begin{bmatrix} -6 & -4l_{ij} & 6 & -2l_{ij} \\ 6 & -2l_{ij} & -6 & 4l_{ij} \end{bmatrix} \begin{bmatrix} w_i & \theta_{ni} & w_j & \theta_{nj} \end{bmatrix}^{\mathrm{T}}. \tag{7}$$

Here, l_{ij} is length of side ij. By appropriately transforming the curvature readings from all three reference directions at a node to the Cartesian curvatures, and similarly transforming from Cartesian rotational degrees of freedom to the reference line normal rotation, one can establish the curvature relationship at a node as

$$\boldsymbol{\kappa}_i = \mathbf{B}_i \mathbf{v} \tag{8}$$

and the assumed curvature distribution is obtained by linear interpolation over the element domain.

The ANDES higher order bending is then computed using the deviatoric part of the curvature displacement relationship

$$\mathbf{K}_{\mathrm{d}} = \int_A \mathbf{B}_{\mathrm{d}} \mathbf{C}_{\mathrm{d}} \mathbf{B}_{\mathrm{d}}^{\mathrm{T}} \, \mathrm{d}A \quad \text{where} \quad \mathbf{B}_{\mathrm{d}} = \mathbf{B} - \frac{1}{A} \int_A \mathbf{B} \, \mathrm{d}A. \tag{9}$$

2.3. Nonlinear kinematics

Fig. 3 shows the two basic coordinate systems that are used. The global coordinate system is represented by unit vectors $\mathbf{I}_1$, $\mathbf{I}_2$ and $\mathbf{I}_3$. The co-rotated element coordinate system shared by shadow configuration C_{0n} and configuration C_n is represented by unit vectors $\mathbf{i}_1^n$, $\mathbf{i}_2^n$ and $\mathbf{i}_3^n$. Vectors given in the local co-rotated element coordinate system are marked with a tilde($\sim$). A vector $\mathbf{x}$ in global coordinates is transformed into a vector $\tilde{\mathbf{x}}$ in the local coordinate system 0 by

$$\tilde{\mathbf{x}} = \mathbf{T}_0 \mathbf{x} \quad \mathbf{T}_0 = \begin{bmatrix} \mathbf{i}_1^{0\mathrm{T}} \\ \mathbf{i}_2^{0\mathrm{T}} \\ \mathbf{i}_3^{0\mathrm{T}} \end{bmatrix}. \tag{10}$$

$\mathbf{T}_0$ is orthonormal. The rigid body rotation of $\mathbf{i}_i^0$ to $\mathbf{i}_i^n$ is given by

$$\mathbf{i}_1^n = \mathbf{R}_{0n} \mathbf{i}_1^0 \quad \mathbf{R}_{0n} = \mathbf{T}_n^{\mathrm{T}} \mathbf{T}_0, \tag{11}$$
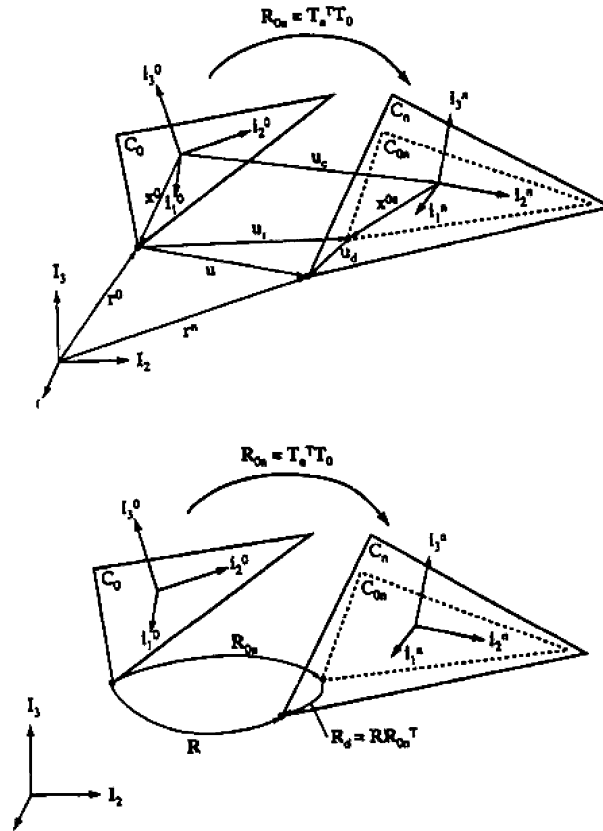
Fig. 3. Co-rotated thin shell kinematics (a triangular element is used for illustration).

where $\mathbf{R}_{0n}$ is the rigid body rotation matrix from position 0 to position n. The Rodrigues representation of the rotation matrix is used. The rotation matrix for a rotation θ about an axis defined by the unit vector $\mathbf{n}^{\mathrm{T}} = [n_1 \ n_2 \ n_3]$ is written [10]

$$\mathbf{R} = \mathbf{I} + \mathbf{N}\sin\theta + \mathbf{N}^2(1 - \cos\theta), \tag{12}$$

$$\mathbf{N} = \mathrm{Spin}(\mathbf{n}) = \begin{bmatrix} 0 & -n_3 & n_2 \\ n_3 & 0 & -n_1 \\ -n_2 & n_1 & 0 \end{bmatrix}$$

$\mathbf{I}$ is the 3×3 identity matrix. Rotation of a vector $\mathbf{r}_0$ into $\mathbf{r}$ through an angle θ about an axis defined by the unit vector $\mathbf{n}$ is obtained by

$$\mathbf{r} = \mathbf{R}\mathbf{r}_0. \tag{13}$$

The displacement vector is given as the difference between the position vector in configuration C_0 and the position vector in configuration C_n.

$$\mathbf{u} = \mathbf{r}^n - \mathbf{r}^0. \tag{14}$$

The displacement vector is split into a deformational displacement vector and a rigid body displacement vector

$$\mathbf{u} = \mathbf{u}_r + \mathbf{u}_d \quad \mathbf{u}_r = \mathbf{r}^{0n} - \mathbf{r}^0 \quad \mathbf{u}_d = \mathbf{r}^n - \mathbf{r}^{0n}. \tag{15}$$

Introducing subscript c for the arithmetic mean of the coordinates of the points in the element, the position vectors in initial and shadow element configurations may be written as:

$$\begin{aligned} \mathbf{r}^0 &= \mathbf{r}_c^0 + \mathbf{x}^0, \\ \mathbf{r}^{0n} &= \mathbf{r}_c^{0n} + \mathbf{x}^{0n} = \mathbf{r}_c^0 + \mathbf{u}_c + \mathbf{R}_{0n}\mathbf{x}^0, \end{aligned} \tag{16}$$

where $\mathbf{x}^0$ and $\mathbf{x}^{0n}$ are the vectors from the centroid of the element to the point being considered in the C_0 configuration and the C_{0n} configuration, respectively. Substitution of the expressions above into Eq. (15) yields

$$\mathbf{u}_d = \mathbf{u} - \mathbf{u}_r = \mathbf{u} - (\mathbf{r}^{0n} - \mathbf{r}^0) = \mathbf{u} - \mathbf{u}_c - (\mathbf{R}_{0n} - \mathbf{I})\mathbf{x}^0. \tag{17}$$

The rotation of an element node as it moves from the initial configuration C_0 to the deformed configuration C_n is described by the rotation matrix $\mathbf{R}$. The rotation matrix is split into a rigid body rotation $\mathbf{R}_{0n}$ and a deformational rotation $\mathbf{R}_d$.

$$\mathbf{R} = \mathbf{R}_d\mathbf{R}_{0n} \tag{18}$$

$$\mathbf{R}_d = \mathbf{R}\mathbf{R}_{0n}^{T} = \mathbf{R}\mathbf{T}_0^{T}\mathbf{T}_n. \tag{19}$$

The deformational rotation matrix transformed into the local coordinate system shared by configurations C_{0n} and C_n reads

$$\widetilde{\mathbf{R}}_d = \mathbf{T}_n\mathbf{R}_d\mathbf{T}_n^{T} = \mathbf{T}_n\mathbf{R}\mathbf{T}_0^{T}. \tag{20}$$

The position of an element node a with initial coordinates $\mathbf{r}_a^0$, is defined by the translational displacement $\mathbf{u}_a$ and the rotational orientation $\mathbf{R}_a$. Together, the set $(\mathbf{u}_a, \mathbf{R}_a)$ for $a = 1, \ldots, N$ is the nodal displacement vector $\hat{\mathbf{v}}$. $\hat{\mathbf{v}}$ is interpreted as an array of numbers that defines the position of the deformed element. In order to establish the force vector and tangent stiffness for an element, the *deformational* vector for the element needs to be established. This vector is denoted $\tilde{\mathbf{v}}_d$ and contains translational and rotational degrees of freedom for each element node ordered as

$$\tilde{\mathbf{v}}_d^{T} = \begin{bmatrix} \tilde{\mathbf{u}}_{d1}^{T} & \tilde{\boldsymbol{\theta}}_{d1}^{T} & \ldots & \tilde{\mathbf{u}}_{dN}^{T} & \tilde{\boldsymbol{\theta}}_{dN}^{T} \end{bmatrix}. \tag{21}$$

N is the number of element nodes for the element being considered. $\tilde{\boldsymbol{\theta}}_d$ is obtained from $\widetilde{\mathbf{R}}_d$.

2.4. Equilibrium and tangent stiffness

2.4.1. Equilibrium
Virtual work is employed as weak form of the equilibrium equations:

$$\begin{aligned} &\delta_R\tilde{\mathbf{v}}_d^{T}\tilde{\mathbf{f}}_e - \delta\mathbf{v}^{T}\mathbf{f}_{ext} = \delta\mathbf{v}^{T}\left[\left(\frac{\partial_R\mathbf{v}_d}{\partial\mathbf{v}}\right)^{T}\mathbf{f}_e - \mathbf{f}_{ext}\right] = 0, \\ &\Rightarrow \mathbf{f}_e = \mathbf{T}^{T}\widetilde{\mathbf{P}}^{T}\widetilde{\mathbf{H}}^{T}\tilde{\mathbf{f}}_e = \mathbf{f}_{ext}. \end{aligned} \tag{22}$$

The transformations are matrices accounting for large rigid body translations and rotations, and are explained briefly in the following, see [5] for details. First, the variation of the transformation matrix with respect to infinitesimal rotations about the local coordinate axes reads

$$\delta\mathbf{T}_n = \frac{\partial\mathbf{T}_n}{\partial\tilde{\omega}_i}\,\delta\tilde{\omega}_i = \begin{bmatrix} 0 & \delta\tilde{\omega}_z & -\delta\tilde{\omega}_y \\ -\delta\tilde{\omega}_z & 0 & \delta\tilde{\omega}_x \\ \delta\tilde{\omega}_y & -\delta\tilde{\omega}_x & 0 \end{bmatrix}\begin{bmatrix} \mathbf{i}_1^{n\mathrm{T}} \\ \mathbf{i}_2^{n\mathrm{T}} \\ \mathbf{i}_3^{n\mathrm{T}} \end{bmatrix} = -\mathrm{Spin}(\delta\tilde{\boldsymbol{\omega}})\mathbf{T}_n. \tag{23}$$

Transformation of $\mathrm{Spin}(\delta\tilde{\boldsymbol{\omega}})$ to global coordinates reads

$$\delta\mathbf{T}_n = -\mathrm{Spin}(\delta\tilde{\boldsymbol{\omega}})\mathbf{T}_n = -\mathbf{T}_n\mathrm{Spin}(\delta\boldsymbol{\omega})\mathbf{T}_n^{\mathrm{T}}\mathbf{T}_n = -\mathbf{T}_n\mathrm{Spin}(\delta\boldsymbol{\omega}). \tag{24}$$

Second, the rotation matrix $\mathbf{R}_{0n}$ rotates a vector from initial configuration to the shadow configuration, hence the variation of the rotation matrix reads

$$\delta\mathbf{R}_{0n} = \delta\mathbf{T}_n^{\mathrm{T}}\mathbf{T}_0 + \mathbf{T}_n^{\mathrm{T}}\delta\mathbf{T}_0 = \delta\mathbf{T}_n^{\mathrm{T}}\mathbf{T}_0 = \mathrm{Spin}(\delta\boldsymbol{\omega})\mathbf{T}_n^{\mathrm{T}}\mathbf{T}_0 = \mathrm{Spin}(\delta\boldsymbol{\omega})\mathbf{R}_{0n}. \tag{25}$$

The variation of a vector expressed in a global frame can be expressed as

$$\delta\mathbf{x} = \delta_{\mathrm{R}}\mathbf{x} + \delta\boldsymbol{\omega}\times\mathbf{x} = \delta_{\mathrm{R}}\mathbf{x} + \mathrm{Spin}(\delta\boldsymbol{\omega})\mathbf{x}, \tag{26}$$

where $\delta_R\mathbf{x}$ is the variation of the vector in the co-rotated frame, and $\delta\boldsymbol{\omega}$ is the variation of the global rotation of the frame. The variation of the *co-rotated* deformational displacement vector $\mathbf{u}_{\mathrm{d}}$ in a co-rotated frame is obtained via the variation of the global deformational displacements with respect to global $\mathbf{v}$, and using Eq. (26) to find the variation of the co-rotated deformational *displacements* with respect to global $\mathbf{v}$. Eq. (17) states that deformational displacement of an element node a is

$$\mathbf{u}_{\mathrm{d}a} = \mathbf{u}_a - \mathbf{u}_c - (\mathbf{R}_{0n} - \mathbf{I})\mathbf{x}_a^0 = \sum_{b=1}^{N}\delta_{ab}\mathbf{u}_{\mathrm{b}} - \sum_{b=1}^{N}\frac{1}{N}\mathbf{u}_{\mathrm{b}} - (\mathbf{R}_{0n} - \mathbf{I})\mathbf{x}_a^0, \tag{27}$$

$\mathbf{u}_c$ is the displacement vector for the element centroid, and δ_{ab} is the Kronecker delta, hence

$$\begin{aligned} \mathbf{u}_{\mathrm{d}a} &= \sum_{b=1}^{N}\mathbf{P}_{ab}\mathbf{u}_{\mathrm{b}} - (\mathbf{R}_{0n} - \mathbf{I})\mathbf{x}_a^0, \\ \mathbf{P}_{ab} &= \left(\delta_{ab} - \frac{1}{N}\right)\mathbf{I}. \end{aligned} \tag{28}$$

The variation of global $\mathbf{u}_{\mathrm{d}a}$ with respect to global $\mathbf{v}$ is found as

$$\delta\mathbf{u}_{\mathrm{d}a} = \sum_{b=1}^{N}\mathbf{P}_{ab}\,\delta\mathbf{u}_{\mathrm{b}} - \delta\mathbf{R}_{0n}\mathbf{x}_a^0. \tag{29}$$

Using Eq. (25) we have

$$\begin{aligned} \delta\mathbf{R}_{0n}\mathbf{x}_a^0 &= \mathrm{Spin}(\delta\boldsymbol{\omega}_{\mathrm{r}})\mathbf{R}_{0n}\mathbf{x}_a^0 = \mathrm{Spin}(\delta\boldsymbol{\omega}_{\mathrm{r}})\mathbf{x}_a^{0n} = -\mathrm{Spin}(\mathbf{x}_a^{0n})\delta\boldsymbol{\omega}_{\mathrm{r}} \\ &= -\mathrm{Spin}(\mathbf{x}_a^{0n})\mathbf{G}\,\delta\mathbf{v}. \end{aligned} \tag{30}$$

The matrix $\mathbf{G}$ connects the variation of the rigid body rotation of the shell element to the variation of the node displacements:

$$\delta\boldsymbol{\omega}_{\mathrm{r}} = \frac{\partial\boldsymbol{\omega}_{\mathrm{r}}}{\partial v_i}\,\delta v_i = \mathbf{G}\,\delta\mathbf{v} = \sum_{b=1}^{N}\mathbf{G}_{\mathrm{b}}\,\delta\mathbf{v}_{\mathrm{b}}. \tag{31}$$

The matrix $\mathbf{G}$ is an element-*type* dependent matrix. The variation of *global* $\mathbf{u}_{\mathrm{d}}$ with respect to global $\mathbf{v}$ then reads

$$\delta\mathbf{u}_{\mathrm{d}a} = \sum_{b=1}^{N}\left(\begin{bmatrix}\mathbf{P}_{ab} & \mathbf{0}\end{bmatrix} + \mathrm{Spin}(\mathbf{x}_a^{0n})\mathbf{G}_{\mathrm{b}}\right)\delta\mathbf{v}_{\mathrm{b}}. \tag{32}$$

$\delta\mathbf{v}_b$ is the global degrees of freedom for node b. Using the relationship $\mathbf{u}_{da} = \mathbf{x}_a^n - \mathbf{x}_a^{0n}$, we find that the variation of the co-rotated deformational displacement vector with respect to global degrees of freedom is given by

$$\delta_R\mathbf{u}_{da} = \delta_R\mathbf{x}_a^n - \delta_R\mathbf{x}_a^{0n} = \delta_R\mathbf{x}_a^n. \tag{33}$$

Since $\mathbf{x}_a^n = \mathbf{R}_{0n}\mathbf{x}_a^0 + \mathbf{u}_{da}$, the variation of global $\mathbf{x}_a^n$ with respect to global degrees of freedom is given by

$$\delta\mathbf{x}_a^n = \delta\mathbf{R}_{0n}\mathbf{x}_a^0 + \mathbf{R}_{0n}\delta\mathbf{x}_a^0 + \delta\mathbf{u}_{da} = \sum_{b=1}^{N}\mathbf{P}_{ab}\,\delta\mathbf{u}_b. \tag{34}$$

Substituting $\mathbf{x}_a^n$ for $\mathbf{x}$ in Eq. (26) and solving with respect to $\delta_R\mathbf{x}_a^n$ yields

$$\delta_R\mathbf{x}_a^n = \sum_{b=1}^{N}\mathbf{P}_{ab}\,\delta\mathbf{u}_b - \mathrm{Spin}(\delta\boldsymbol{\omega}_r)\mathbf{x}_a^n = \sum_{b=1}^{N}\mathbf{P}_{ab}\,\delta\mathbf{u}_b + \mathrm{Spin}(\mathbf{x}_a^n)\delta\boldsymbol{\omega}_r = \sum_{b=1}^{N}\big([\mathbf{P}_{ab} \quad \mathbf{0}] + \mathrm{Spin}(\mathbf{x}_a^n)\mathbf{G}_b\big)\delta\mathbf{v}_b. \tag{35}$$

Hence, we have the variation of co-rotated deformational displacement vector with respect to global degrees of freedom $\delta_R\mathbf{u}_{da} = \delta_R\mathbf{x}_a^n$.

By starting with the variation of the co-rotated deformational rotations with respect to global degrees of freedom, the variation of the co-rotated deformational (finite) rotations with respect to the co-rotated deformational (infinitesimal) rotations is obtained. The derivation is based on [11–13].

$$\delta_R\boldsymbol{\theta}_{da} = \frac{\partial\boldsymbol{\theta}_{da}}{\partial\boldsymbol{\omega}_{da}}\delta_R\boldsymbol{\omega}_{da} = \frac{\partial(\mathrm{Axial}(\ln(\mathbf{R}_{da})))}{\partial\boldsymbol{\omega}_{da}}\delta_R\boldsymbol{\omega}_{da} = \mathbf{H}_a\delta_R\boldsymbol{\omega}_{da}, \tag{36}$$

$$\mathbf{H}_a = \frac{\partial\boldsymbol{\theta}_a}{\partial\boldsymbol{\omega}} = \mathbf{I} - \frac{1}{2}\mathrm{Spin}(\boldsymbol{\theta}_a) + \eta\,\mathrm{Spin}(\boldsymbol{\theta}_a)^2, \tag{37}$$

$$\eta = \frac{\sin(\frac{1}{2}\theta_a) - \frac{1}{2}\theta_a\cos(\frac{1}{2}\theta_a)}{\theta_a^2\sin(\frac{1}{2}\theta_a)} \quad \text{and} \quad \theta_a = \sqrt{\boldsymbol{\theta}_a^T\boldsymbol{\theta}_a} = \|\theta_a\| \tag{38}$$

$$\delta_R\boldsymbol{\omega}_{da} = \delta\boldsymbol{\omega}_a - \delta\boldsymbol{\omega}_r = \delta\boldsymbol{\omega}_a - \frac{\partial\boldsymbol{\omega}_r}{\partial v_i}\delta v_i = \delta\boldsymbol{\omega}_a - \mathbf{G}_a\,\delta\mathbf{v}_a. \tag{39}$$

$\mathbf{G}$ is defined in Eq. (31). $\delta_R\boldsymbol{\omega}_{da}$ a may now be written as

$$\delta_R\boldsymbol{\omega}_{da} = \sum_{b=1}^{N}\big(\delta_{ab}[\mathbf{0} \quad \mathbf{I}] - \mathbf{G}_b\big)\delta\mathbf{v}_b. \tag{40}$$

Introducing Eq. (32) into Eq. (36) yields the final expression for the variation of co-rotated deformational rotation with respect to global degrees of freedom.

$$\delta_R\boldsymbol{\theta}_{da} = \mathbf{H}_a\sum_{b=1}^{N}\big(\delta_{ab}[\mathbf{0} \quad \mathbf{I}] - \mathbf{G}_b\big)\delta\mathbf{v}_b. \tag{41}$$

For an element with N nodes, the nodal degrees of freedom are ordered as follows:

$$\mathbf{v}^T = \begin{bmatrix}\mathbf{u}_1^T & \boldsymbol{\theta}_1^T & \dots & \mathbf{u}_N^T & \boldsymbol{\theta}_N^T\end{bmatrix}. \tag{42}$$

If Eqs. (35) and (41) are ordered accordingly, $\delta_R\mathbf{v}_d$ (containing both displacements and rotations) may be written as

$$\delta_R\mathbf{v}_d = \mathbf{H}(\mathbf{I} - \mathbf{P}_T - \mathbf{P}_R)\delta\mathbf{v} = \mathbf{HP}\,\delta\mathbf{v}. \tag{43}$$

Matrix $\mathbf{P}$ is a nonlinear projector operator that filters out rigid body translation and rotation.

The variation of the co-rotated deformational displacement vector has now been found with respect to a set of global degrees of freedom. To enable use of existing linear elements put in the rotating frame, the global system is chosen to be that of the co-rotated element. Thus, Eq. (43) is modified to

$$\delta_R \tilde{\mathbf{v}}_d = \widetilde{\mathbf{H}} \widetilde{\mathbf{P}} \, \delta \tilde{\mathbf{v}}. \tag{44}$$

Taking advantage of the transformation between local and global coordinate system, we have

$$\delta_R \tilde{\mathbf{v}}_d = \widetilde{\mathbf{H}} \widetilde{\mathbf{P}} \mathbf{T}_n \, \delta \mathbf{v}. \tag{45}$$

2.4.2. Tangent stiffness

The consistent tangent stiffness is obtained by the variation of the internal force vector $\mathbf{f}_e$ with respect to $\mathbf{v}$:

$$\delta \mathbf{f}_e = \frac{\partial \mathbf{f}}{\partial \mathbf{v}} \, \delta \mathbf{v} = \mathbf{K}_t \, \delta \mathbf{v}. \tag{46}$$

Using Eq. (22) for $\mathbf{f}_e$, Eq. (46) yields

$$\begin{aligned}
\delta \mathbf{f} &= \delta \mathbf{T}^T \widetilde{\mathbf{P}}^T \widetilde{\mathbf{H}}^T \tilde{\mathbf{f}}_e + \mathbf{T}^T \delta_R \widetilde{\mathbf{P}}^T \widetilde{\mathbf{H}}^T \tilde{\mathbf{f}}_e + \mathbf{T}^T \widetilde{\mathbf{P}}^T \delta_R \widetilde{\mathbf{H}}^T \tilde{\mathbf{f}}_e + \mathbf{T}^T \widetilde{\mathbf{P}}^T \widetilde{\mathbf{H}}^T \delta \tilde{\mathbf{f}}_e \\
&= (\mathbf{K}_{GR} + \mathbf{K}_{GP} + \mathbf{K}_{GM} + \mathbf{K}_{MG}) \delta \mathbf{v} = \mathbf{K}_T \, \delta \mathbf{v}.
\end{aligned} \tag{47}$$

The different terms of the tangent stiffness represent rotational geometric stiffness, projection geometric stiffness, moment correction geometric stiffness, and material stiffness, respectively.

The rotational geometric stiffness arises from the variation of the transformation matrix between initial configuration C_0 and shadow configuration C_n. As a rigid rotation of a stressed element rotates the stresses, the internal forces change direction to preserve equilibrium.

The equilibrium projection geometric stiffness arises from the variation of the projector matrix $\widetilde{\mathbf{P}}^T$, and reflects the variation of the force vector due to variations in the degrees of freedom.

The moment correction geometric stiffness arises from variation of the rotation pseudo-vector Jacobian $\widetilde{\mathbf{H}}$.

2.4.3. Elastic–plastic stiffness

$\widetilde{\mathbf{K}}_e$ represents the material stiffness for the element, and may include plasticity effects. It connects the local deformational dof increment with the local force increment

$$\delta \tilde{\mathbf{f}}_e = \widetilde{\mathbf{K}}_e \delta_R \tilde{\mathbf{v}}_d. \tag{48}$$

A stress resultants yield criterion based on Ilyushin [14] is employed for the shell element. For thin shells of materials with plastic yielding governed by the Mises yield criterion, the Ilyushin criterion works well. Denoting the integration point stress resultant vector by $\boldsymbol{\sigma} = [\tilde{\boldsymbol{n}}, \tilde{\boldsymbol{m}}]^T$ the isotropic yield criterion is rewritten in quadratic form [15,16]:

$$\begin{aligned}
& f = \boldsymbol{\sigma}^T A \boldsymbol{\sigma} - \left(1 + \frac{H \epsilon_p}{\sigma_y}\right)^2 = 0, \\[2mm]
& A = \begin{bmatrix} \dfrac{1}{n_0^2} \overline{A} & \dfrac{s}{2\sqrt{3} m_0 n_0} \overline{A} \\[3mm] \dfrac{s}{2\sqrt{3} m_0 n_0} \overline{A} & \dfrac{1}{m_0^2} \overline{A} \end{bmatrix}, \quad \overline{A} = \begin{bmatrix} 1 & -0.5 & 0 \\ -0.5 & 1 & 0 \\ 0 & 0 & 3 \end{bmatrix}, \\[2mm]
& m_0 = 0.25 \sigma_y t^2, \quad n_0 = \sigma_y t.
\end{aligned} \tag{49}$$

The stress resultant vector $\boldsymbol{\sigma}$ and the differential plastic strain vector $\mathrm{d}\boldsymbol{\epsilon}_\mathrm{p}$ are related to the equivalent stress and equivalent plastic strain increment by the relation

$$\boldsymbol{\sigma}^\mathrm{T}\mathrm{d}\boldsymbol{\epsilon}_\mathrm{p} = \bar{\sigma}\mathrm{d}\bar{\epsilon}_\mathrm{p} \Rightarrow \mathrm{d}\bar{\epsilon}_\mathrm{p} = 2\bar{\sigma}\mathrm{d}\lambda \quad \bar{\sigma} = \sqrt{\boldsymbol{\sigma}^\mathrm{T}A\boldsymbol{\sigma}} \tag{50}$$

The following power law work hardening model is employed:

$$\bar{\sigma} = \sigma_\mathrm{y}\left(\frac{\bar{\epsilon}_\mathrm{p}}{\epsilon_\mathrm{y}} + 1\right)^n, \tag{51}$$

where $\sigma_\mathrm{y} = E\epsilon_\mathrm{y}$ and n is the hardening exponent ($0 \leqslant n < 1$). Utilising an associated flow rule, the backward Euler update of the plastic strain increment reads

$$\Delta\boldsymbol{\epsilon}_{\mathrm{p},n+1} = \Delta\lambda_{n+1}\frac{\partial f}{\partial\boldsymbol{\sigma}_{n+1}} \quad \Delta\boldsymbol{\epsilon} = [\Delta\boldsymbol{\epsilon}_m, \Delta\boldsymbol{\kappa}]^\mathrm{T}. \tag{52}$$

Here $n + 1$ corresponds to the current load step in the global Newton–Raphson equilibrium iteration. In the elastic predictor plastic corrector approach applied herein, the stress update is obtained by

$$\boldsymbol{\sigma}_{n+1} = \boldsymbol{\sigma}_\mathrm{trial} - C\Delta\boldsymbol{\epsilon}_{\mathrm{p},n+1} = \overline{\boldsymbol{Q}}^{-1}\boldsymbol{\sigma}_\mathrm{trial}, \quad \overline{\boldsymbol{Q}} = [\boldsymbol{I} + 2\Delta\lambda CA],$$

$$\boldsymbol{C} = \begin{bmatrix} t\boldsymbol{D} & 0 \\ 0 & \frac{t^3}{12}\boldsymbol{D} \end{bmatrix}, \quad \boldsymbol{D} = \frac{E}{1-v^2}\begin{bmatrix} 1 & v & 0 \\ v & 1 & 0 \\ 0 & 0 & \frac{1-v}{2} \end{bmatrix}.$$

The discrete yield condition f_{n+1} now depends only on $\Delta\lambda$. Solving for $f(\Delta\lambda_{n+1})$ (Newton–Raphson) the stress update is obtained. The consistent material tangent for an integration point reads

$$\mathrm{d}\boldsymbol{\sigma} = \left[\boldsymbol{H} - \frac{\boldsymbol{H}\boldsymbol{g}\boldsymbol{g}^\mathrm{T}\boldsymbol{H}}{\boldsymbol{g}^\mathrm{T}\boldsymbol{H}\boldsymbol{g} + \beta}\right]\mathrm{d}\boldsymbol{\epsilon} = \boldsymbol{C}_t\mathrm{d}\boldsymbol{\epsilon},$$

$$\beta = \frac{2\alpha\bar{\sigma}}{1 - \alpha\frac{\Delta\lambda}{\bar{\sigma}}} \quad \alpha = \frac{2H}{\sigma_\mathrm{y}^2}(\sigma_\mathrm{y} + H\epsilon_{\mathrm{p},n+1}), \tag{53}$$

$$\boldsymbol{H}^{-1} = \boldsymbol{C}^{-1} + 2\Delta\lambda A \quad \boldsymbol{g} = 2A\boldsymbol{\sigma}.$$

2.4.4. Solution procedure

The balance equation between internal and external forces for the assembled element model during a load step from state n to $n + 1$ reads

$$\boldsymbol{K}\Delta\mathbf{v} = \mathbf{f}_\mathrm{ext}^\mathrm{pre} + \lambda\mathbf{f}_{\mathrm{ext},\lambda=1}(\mathbf{v}) - \mathbf{f}_\mathrm{int}(\mathbf{v}). \tag{54}$$

The structure may be preloaded with the load vector $\mathbf{f}_\mathrm{ext}^\mathrm{pre}$. In case of nonconservative loading (e.g. pressure) this vector is a function of the current configuration. No limit points must be reached during the preloading. The preloading is followed by an external loading expressed by the load parameter λ. In the LINK program the following simple method is used to go from state n to state $n + 1$: one characteristic degree of freedom is given a specified incremental value, then the corresponding load parameter λ and all other DOF are computed based on the current configuration at state n such that Eqn. (54) is satisfied. The load step is computed using Newton–Raphson iterations until norms of both incremental displacements and unbalanced forces are sufficiently small. During the equilibrium iterations the value of the specified degree of freedom is kept constant whereas updated values of λ are computed based on updated configurations of state $n + 1$. The procedure is a subset of the hyperplane control described by Bergan and Simons [17].

The update of the global displacement and rotation is obtained as follows:

displacements: $\quad \mathbf{u} := \mathbf{u} + \Delta\mathbf{u}$, \hfill (55)

rotations: $\quad \mathbf{R} := \mathbf{R}(\Delta\omega)\mathbf{R}$. \hfill (56)

3. Linespring finite element

The part-through surface crack is originally a three dimensional problem. The three dimensional problem is formulated within the context of two-dimensional plate or shell theory with the part-cracked section represented as a linespring. The linesprings take into account the additional flexibility due to the surface crack. The linespring element can be schematically represented by two straight lines connected to each other by a series of springs. At zero deformation the lines lie upon each other. When a Mode I (crack opening) deformation takes place each line displaces in opposite direction. The displacement and rotation are constrained by the springs. As the shell element used herein is 4-noded, the linespring element is 4-noded with linear interpolation polynomials. A 2-point Gauss integration is employed. Hence, the linespring element has 8 degrees of freedom (four in-plane displacements and four rotations with axis along the element), see Fig. 4.

The general yield surfaces ϕ governing the plastic behavior of cracked shell section ligament is plotted in the generalized force space $Q_{1,2}$ for different crack depth to thickness ratios $\frac{a}{h}$, Fig. 5. ϕ contains more accurate information about the general yielding behavior of shallow, as well as deep cracks, for the single edge cracked (SEC) specimen than the typically employed yield surfaces. The stiffness of the linespring, with local extensional and rotational degrees of freedom (Δ, θ), is derived from a plane strain edge-cracked strip loaded in tension and in bending (N, M), i.e. mode I. For a homogeneous material, the general yield surfaces ϕ, governing the plastic behavior of cracked shell section ligament reads

$$\phi = \begin{cases} \phi_{\mathrm{df}}: & \overline{Q}_1 \geqslant \overline{Q}_2 \tan\left(\frac{\pi}{2} + \alpha\right), \\ \phi_{\mathrm{df}}^s: & \overline{Q}_1 < \overline{Q}_2 \tan\left(\frac{\pi}{2} + \alpha\right), \end{cases} \tag{57}$$

where ϕ_{df} is a parabolic yield surface with a validity confined mainly to the I and IV quadrants of the generalized force space, Fig. 5. It reads

$$\phi_{\mathrm{df}} = A\overline{Q}_2 + B\overline{Q}_1 + C\overline{Q}_1^2 + D = 0, \tag{58}$$

see [7] for the fitting parameters A, B, C, D. The function ϕ_{df}^s, symmetric to ϕ_{df} with respect to the line $\overline{Q}_1 = \tan(\frac{\pi}{2} + \alpha)\overline{Q}_2$, can be used in order to describe simplified (conservative) yielding behavior in the II and III quadrants, see Fig. 5.
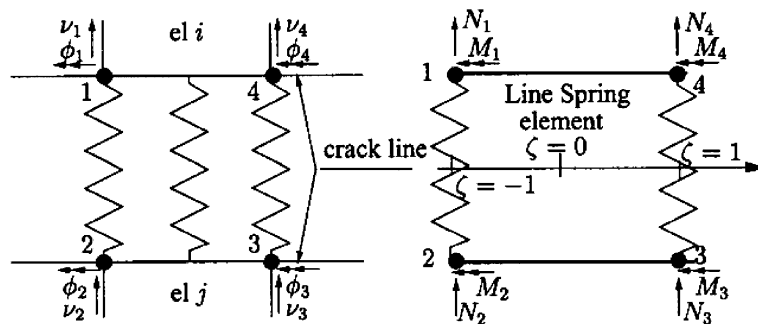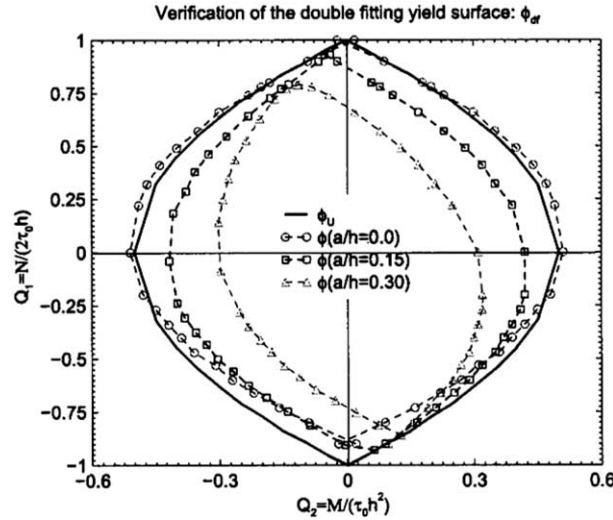

Fig. 4. Linespring finite element.

Fig. 5. Linespring yield surface (Q_1 is normalised membrane force and Q_2 is normalised bending moment).

The angle α between the symmetry line and the Q_1-axis is found to be close to a linear function of the relative crack depth $\frac{a}{h}$. The fitted yield surfaces represented in Fig. 5 were obtained from finite element limit-load analysis results in [18], see [7].

Table 1 lists the main equations for the linespring model at a given integration point in the element. A work hardening model is used. $\mathbf{D}_e$ is the elastic stiffness matrix for the linespring element at an integration point, $d\mathbf{q}$ is the increment in relative opening and rotation of the linespring at the integration point. The functions g_T and g_B are the standard geometry corrections for a finite crack depth in a surface cracked strip [20]. The connection between the elastic J-integral and the mode I stress intensity factor K_I is given along with the link between incremental plastic J and incremental plastic CTOD. The J-integral [21] is a path

Table 1
Basic relationships in line spring model

Yield surface	$\phi(\overline{Q}_1, \overline{Q}_2, \sigma_y; c) = \begin{cases} \phi_{df} & \overline{Q}_1 \geqslant \overline{Q}_2 \tan\left(\frac{\pi}{2} + \alpha\right) \\ \phi_{df}^s & \overline{Q}_1 < \overline{Q}_2 \tan\left(\frac{\pi}{2} + \alpha\right) \end{cases}$
	$Q_1 = N \quad Q_2 = M$
	$\overline{Q}_1 = \frac{N}{2\tau_0 h} \quad \overline{Q}_2 = \frac{M}{\tau_0 h^2} \quad c = h - a$
Work hardening	$dW_p = \mathbf{Q}^T d\mathbf{q}_p = \int_{A_{plastic}} \sigma_{eq} d\epsilon_{p,eq} \, dA = k\sigma_y \frac{d\sigma_y}{E_p} c^{n'}$
Continuum tangent	$d\mathbf{Q} = \left(\mathbf{D}_e - \dfrac{\left(\dfrac{\partial \phi^T}{\partial \mathbf{Q}} \mathbf{D}_e\right)^T \left(\dfrac{\partial \phi^T}{\partial \mathbf{Q}} \mathbf{D}_e\right)}{\dfrac{\partial \phi^T}{\partial \mathbf{Q}} \mathbf{D}_e \dfrac{\partial \phi}{\partial \mathbf{Q}} - \dfrac{\partial \phi^T}{\partial \mathbf{Q}} \mathbf{Q} \dfrac{\partial \phi}{\partial \sigma_y} \dfrac{E_p}{\sigma_y k c^{n'}}} \right) d\mathbf{q}$
	$d\mathbf{Q} = \begin{bmatrix} dQ_1 \\ dQ_2 \end{bmatrix} \quad d\mathbf{q} = \begin{bmatrix} d\Delta \\ d\theta \end{bmatrix}$
Elastic J-integr.	$J_e = \frac{K_I^2}{E'} \quad K_I = \tau_0 h^{\frac{1}{2}}\left[2\overline{Q}_1 g_T\left(\frac{a}{h}\right) + 6\overline{Q}_2 g_B\left(\frac{a}{h}\right)\right]$
Plastic J-integr.	$dJ_{I,p} = m\sigma_y \, d\delta_{I,cracktip,p}$
CTOD vs linespr. deformation	$d\delta_{I,cracktip,p} = d\Delta_p + \left(\frac{t}{2} - a\right)d\theta_p$

independent integral that scales the magnitude of crack tip stress levels, whereas the crack tip opening displacement describes the local crack tip deformation.

Both a forward and backward Euler linespring force update method are implemented in LINK. In the present simulations the forward difference was employed.

4. Numerical simulations

In this section we start with simulation of a test specimen geometry, denoted single edge notched tensile (SENT). This is a very simple and convenient test specimen, but as the simulations show, the physics involved pose major challenges to the linespring formulation. Then tensile loaded cylindrical shells are analysed. Finally some cases of tubulars subjected to bending are analysed. In these simulations the effect of the crack (on the tension side) and geometry effects such as ovalisation and local buckling are investigated.

4.1. Single edged notched tensile (SENT) specimen

This specimen, shown in Fig. 6, has received increased attention as a more representative specimen for fracture mechanics testing in order to obtain low constraint toughnesses. The traditional three-point bend specimen has a high constraint leading to low fracture toughness values. In many structural applications the shell stresses are more dominated by membrane forces, hence, in this situation the SENT specimen is more relevant [19]. As a numerical test case for the linespring formulation it has shown to be a tough one. The main deformation of this "shell" structure is governed by the cracked section, i.e. the linespring. But additionally, when this specimen is pulled to large deformations it shows a "bulging" effect (a nonlinear geometry effect as the center of the ligament is trying to align with the center of the thickness of the surrounding uncracked shell). In addition, and working in an opposite direction of the bulging effect, another nonlinear geometry effect that softens the response develops: the ligament gets smaller as the global shell straining increases. Fig. 7 illustrates a section of the shell and crack. The ligament is crack depth subtracted from the shell thickness. A simple model to account for ligament necking is implemented in the present linespring model. Hence, even for this simple case, nonlinear geometry plays a part in addition to plasticity. The specimen was discretized with five shell elements on each side of the crack, and one line spring element is sufficient for this constant crack depth defect. The crack depth to thickness ratio is 0.2, and the hardening exponent is 0.1.

Fig. 8 depicts the global load versus elongation of the specimen. Note that along the sides the shell elements were constrained to a plane strain condition. The specimen is subjected to a controlled axial displacement at the ends and is fixed with respect to rotation around the y-axis. Very detailed plane strain meshes were employed in the ABAQUS simulations. The legend 2D_ LS is the ABAQUS large strain analysis (SS
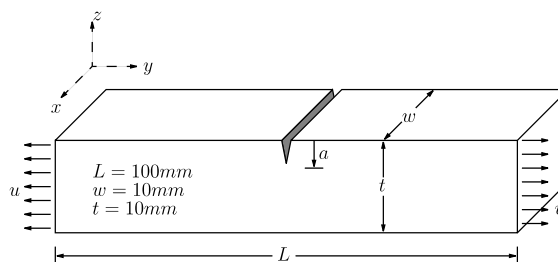

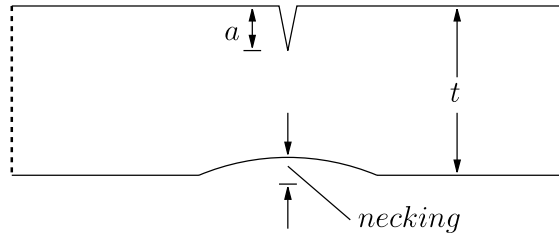Fig. 6. Single edge cracked tensile specimen.
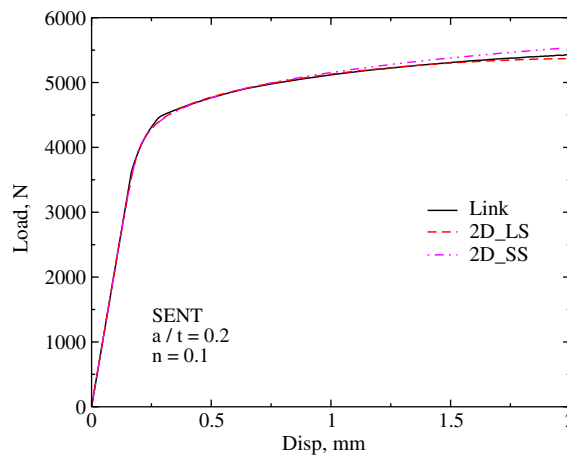
Fig. 7. Ligament necking.

Fig. 8. Load–displacement curve for the SENT specimen.

denotes small strain analysis). It is noted that there is a difference between the large and small strain simulations as a combination of whether or not one accounts for bulging and ligament necking. It is noted that the necking effect dominates as the small strain analysis is above the large strain analysis. The LINK simulation corresponds well with the large strain ABAQUS simulation.

In Fig. 9 the corresponding evolution of CTOD versus elongation is illustrated. Here the difference between the large and small strain ABAQUS anlyses is significant (the small strain simulation being nonconservative). The correspondence between LINK and ABAQUS large strain analysis is good in the range plotted. But it is noted that for larger CTOD values the ABAQUS result is higher than in the LINK simulation. This is due to the fact that the ligament necking accelerates at these high levels, whereas this is not at present accounted for in the linespring model. But the initial CTOD range is well predicted. So as a first attempt the simple linear ligament necking model is acceptable. It can also be noted that for actual metals, higher CTOD values than e.g. 1.5 mm is unrealistic (at this point complete specimen fracture or ductile tearing has occurred).

4.2. Cracked cylindrical shell in tension

The finite element meshes applied for this case are illustrated in Fig. 1. Quarter model symmetry was utilised in the solid finite element model. The global tension load versus nominal axial strain is plotted
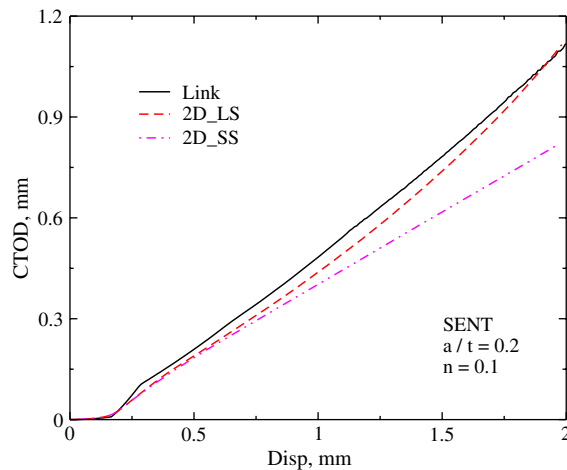
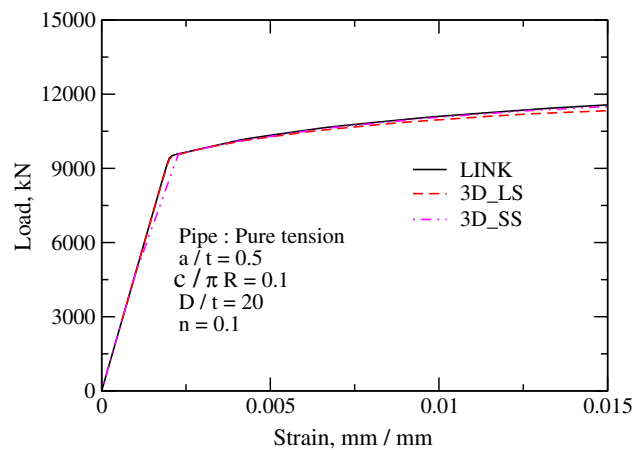Fig. 9. Displacement versus ctod for the SENT specimen.

Fig. 10. Cylindrical shell in tension, global response.

in Fig. 10. The crack size is 50% of the thickness at deepest point and the width of the crack is 10% of the circumference. The relatively high hardening of $n = 0.1$ is employed. No significant difference between the three simulations is noted. In Fig. 11 the CTOD at deepest point versus nominal axial strain is depicted. In the range plotted an acceptable (conservative) response is obtained with LINK. Also here the significant necking effect is noted in the large strain ABAQUS simulation for CTOD values above 2.5 mm. But the LINK prediction is better than the small strain simulation. And as mentioned in the previous section, assuming a stationary crack for a CTOD higher than 1.5 mm is not realistic.

Fig. 12 shows the effect of crack width on the computed CTOD values. The width is either 4% or 10% of the circumference. The correspondence between the detailed large strain solid finite element simulation and the shell/linespring model simulation is very good.
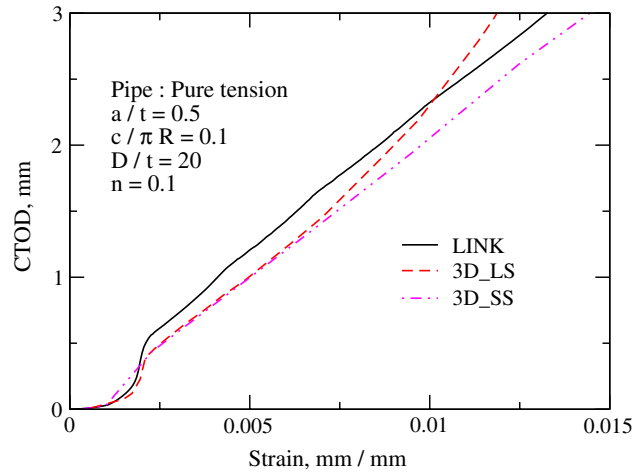
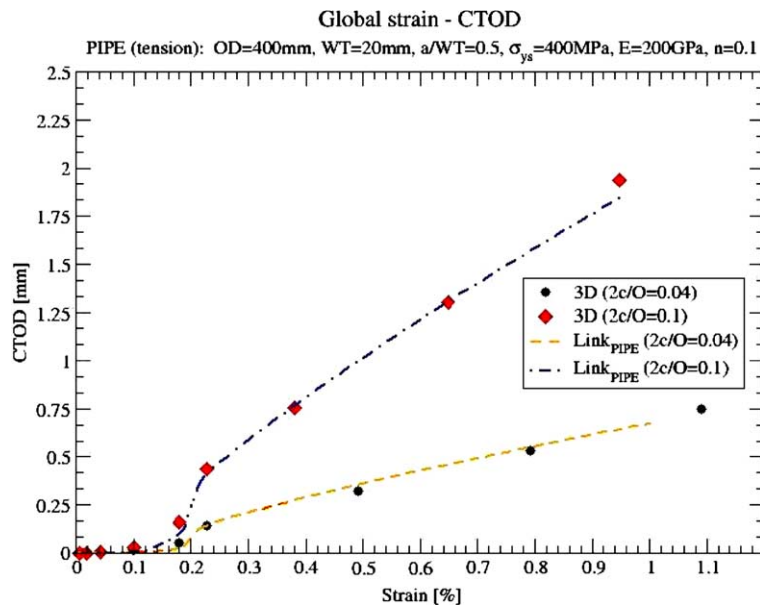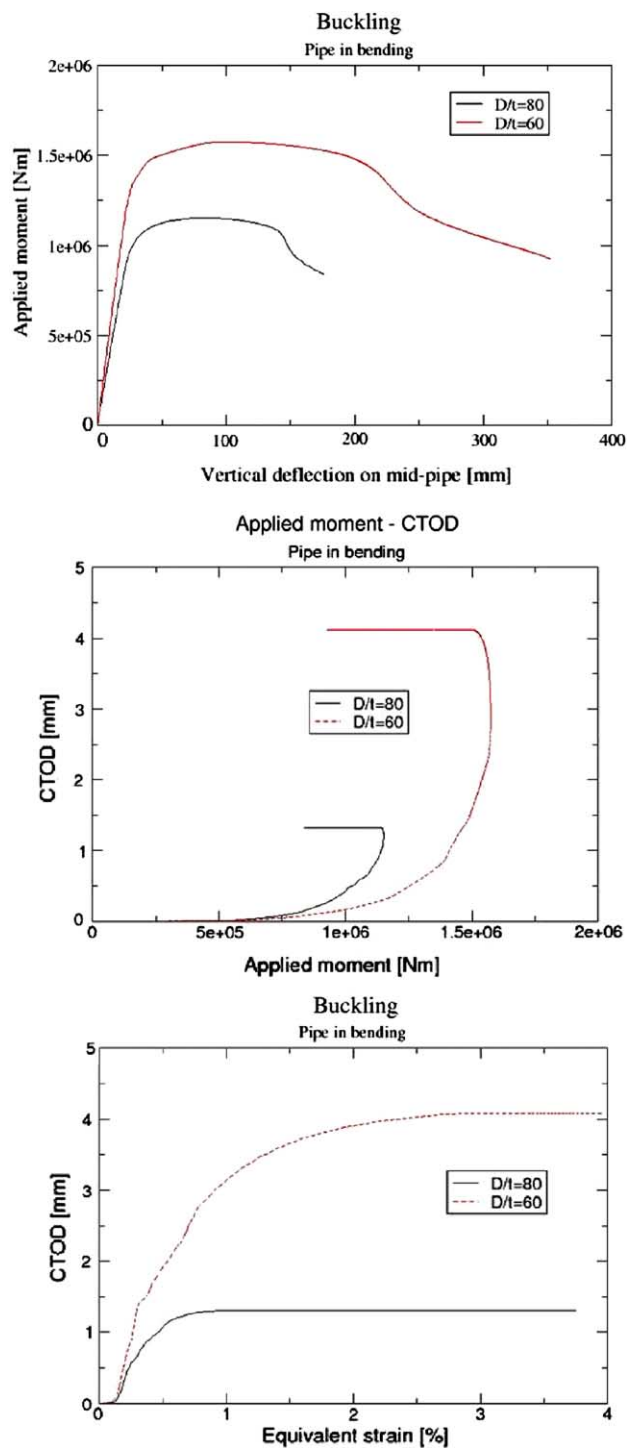Fig. 11. Cylindrical shell in tension, local response.

Fig. 12. Effect of crack width on CTOD for cylindrical shell in tension.

4.3. Cracked cylindrical shell in bending

In Fig. 13 two LINK simulation results are plotted. It is two cylindrical shells subjected to pure bending. The slenderness is relatively high, with outer pipe diameter to shell thickness ratios (D/t) of 60 and 80, respectively. A clear local buckling response is seen in of both the bending moment versus medlength deflection curves. The middle plot shows the CTOD evolution as a function of global bending moment. The effect of local buckling is clearly seen as the CTOD values saturate when local buckling occurs. The bottom graph

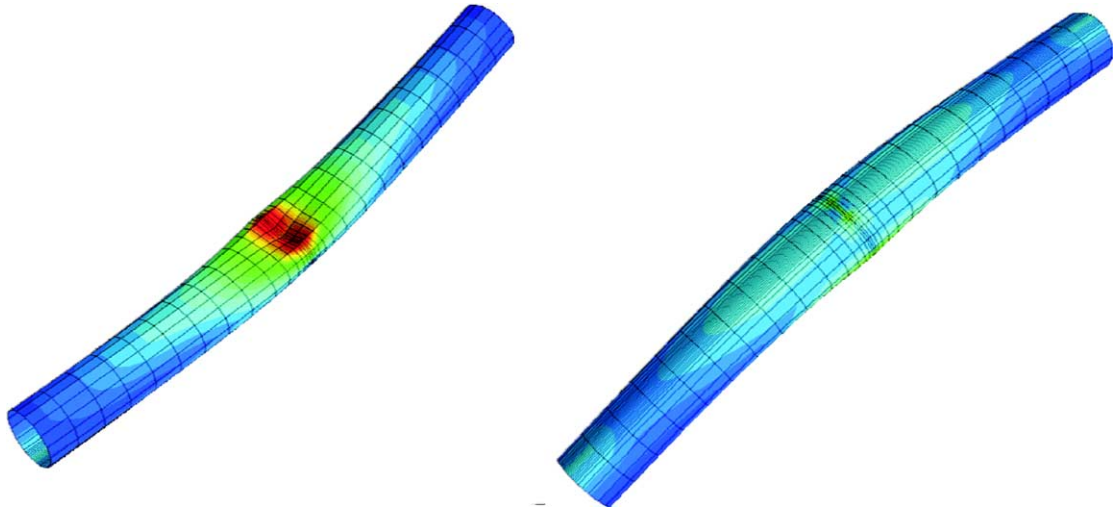Fig. 13. LINK simulations, cylindrical shell in bending, D/t = 60 and 80.

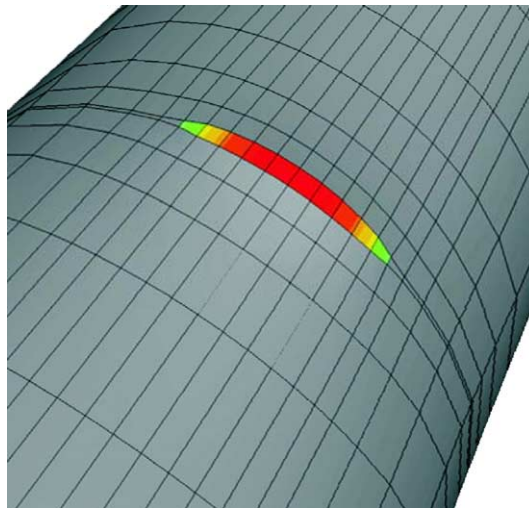Fig. 14. Visualisation of local buckle on compressive side and crack on tensile side.

Fig. 15. Visualisation of CTOD.

shows the CTOD (representing the utilisation on the tension side of the shell) versus the equivalent plastic strain in the local buckle. Such graphs can be used in assessing which of the competing failure modes (fracture or local buckling) occurs first. Considering the pipe with $D/t = 80$, if the measured critical CTOD was higher than 1.5 mm, then local buckling would be the mode defining failure. But if it was e.g. 1 mm, fracture would set the capacity level. Fig. 14 illustrates the corresponding deformed geometry, and Fig. 15 shows the CTOD utilisation along the crack.

Fig. 16 depicts the bending moment versus rotation for a tubular shell with low slenderness, $D/t = 20$. Also here a limit point behavior is observed. This is due to ovalisation instability. The correspondence
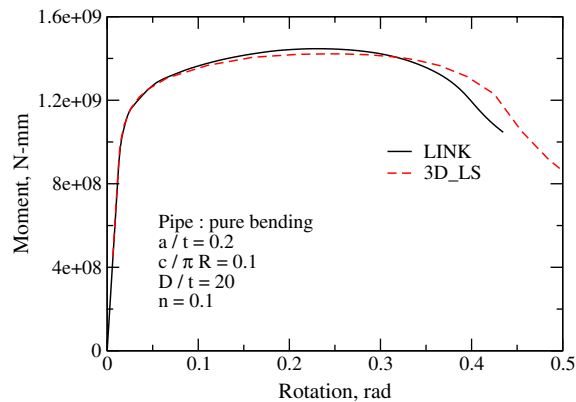
Fig. 16. Cylindrical shell in bending, $D/t = 20$, comparison between solid and shell finite element simulation, global response.
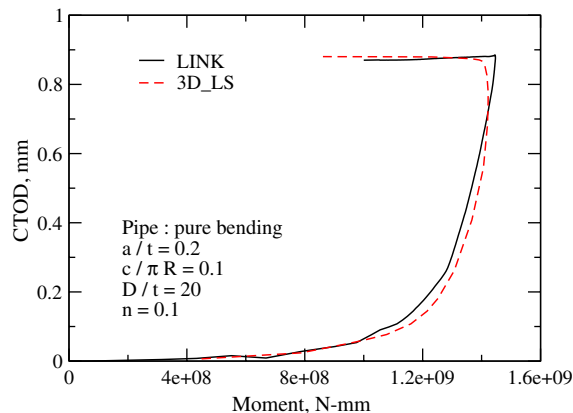

Fig. 17. Cylindrical shell in bending, $D/t = 20$, comparison between solid and shell finite element simulation, local response.

between the LINK and ABAQUS simulation is good. Fig. 17 shows a very good correspondence between the simulations. The saturation of CTOD due to a global instability is clearly observed.

5. Concluding remarks

The present study shows that the combination of co-rotated thin shell elements based on assumed natural deviatoric strains and co-rotated linespring finite elements works well. The possibility to do nonlinear fracture mechanics assessments and shell buckling/instability analyses in a single simulation is convenient. Using current commercial codes on the same problems usually leads to the need of choosing solid finite element modelling. Although accurate results relevant for fracture assessments are obtained, the preparation of the models and extracting the relevant results are cumbersome.

The simple displacement control procedure employed herein with the global Newton–Rapshon iterations will be improved in the near future. Here the orthogonal trajectory method is attractive [27]. The linespring element has to be improved to account for the accelerated necking of the ligament in order to predict more

accurate CTOD values for extremely high utilisations. The linespring does at present not account for ductile tearing. This is a very relevant situation in practical applications, and will be dealt with in the next version of the code. The choice of using a forward Euler linespring force update (and the continuum tangent instead of the consistent tangent) was made for two reasons. First, most of the degrees of freedom stem from the shell finite elements (here consistent linerarisation is employed). The number of linespring dof is small. Hence, it does not slow down the global iterations unacceptably. Second, the linespring yield surface is rather complicated, consisting of several corners in addition to the update of the yield surface size due to ligament necking. Hence, using the explicit time stepping is a pragmatic choice to simplify the implementation.

Acknowledgement

References

[1] J.R. Rice, N. Levy, The part through surface crack in an elastic plate, J. Appl. Mech. (1972) 185–194.
[2] J.R. Rice, The line spring model for surface flaws, in: J.L. Sweldow (Ed.), The Surface Crack Physical Problems and Computer Solutions, ASME, New York, 1972.
[3] D.M. Parks, C.S. White, Elastic–plastic linespring finite element formulation, J. Pressure Vessel Tech. 104 (1982) 287–292.
[4] B. Skallerud, Numerical analysis of cracked inelastic shells under large deformation or mixed mode loading, Int. J. Solids Struct. 56 (1999) 25–40.
[5] B. Skallerud, B. Haugen, Collapse of thin shell structures—stress resultant plasticity modelling within a co-rotated ANDES finite element formulation, Int. J. Numer. Methods Engrg. 36 (1999) 1961–1986.
[6] B. Haugen, Buckling and stability problems for thin shell structures using high performance finite elements, Ph.D. Thesis, Department of Aerospace Engineering, University of Colorado, 1994.
[7] M. Chiesa, B. Skallerud, D. Gross, Closed form line spring yield surfaces for deep and shallow cracks: formulation and numerical performance, Comput. Struct. 80 (2002) 533–545.
[8] Hibbit, Karlson, Sorenson. Abaqus Manuals, version 6.3.
[9] B. Skallerud, B. Haugen, Simplified stress resultant plasticity modelling in collapse analysis of thin shells, in: W. Wunderlich (Ed.), European Conference on Computational Mechanics ECCM'99 CD-ROM, Munchen, 1999.
[10] J.H. Argyris, An excursion into large rotations, Comput. Methods Appl. Mech. Engrg. 32 (1985) 85–155.
[11] B. Nour-Omid, C.C. Rankin, Finite rotation analysis and consistent linearization using projectors, Comput. Methods Appl. Mech. 93 (1991) 353–384.
[12] J.C. Simo, A finite strain beam formulation. The three dimensional dynamic problem. Part I, Comput. Methods Appl. Mech. Engrg. 49 (1985) 55–70.
[13] M.L. Szwabowicz, Variational formulation in the geometrically non-linear thin elastic shell theory, Int. J. Solids Struct. 22 (1986) 1161–1175.
[14] A.A. Ilyushin, Plasticite, Editions Eyrolles, Paris, 1956.
[15] A. Ibrahimbegivic, F. Frey, Stress Resultant Elasto-plastic Analysis of Plates and Shallow Shells, COMPLAS-3, Barcelona, 1992, 2047–2059.
[16] H. Matthies, A decomposition method for integration of elastic–plastic rate problem, Int. J. Numer. Methods Engrg. 28 (1989) 1–11.
[17] P.G. Bergan, J. Simons, Hyperplane displacement control methods in nonlinear analysis, in: W.K. Liu, T. Belytschko, K.C. Park (Eds.), Innovative Methods for Nonlinear Problems, Pineridge Press, Swansea, 1984, pp. 345–364.
[18] H. Lee, D.M. Parks, Fully plastic analysis of plane strain single edged cracked specimen subjected to combined tension and bending, Int. J. Fract. 63 (1993) 329–349.
[19] M. Chiesa, B. Nyhus, B. Skallerud, C. Thaulow, Efficient fracture assessment of pipelines. A constraint corrected SENT specimen approach, Engrg. Fract. Mech. 68 (2001) 527–547.
[20] H. Tada, P.C. Paris, G.R. Irwin, The Stress Analysis of Cracks Handbook, Paris Productions Inc., St Louis, 1985.

[21] J.R. Rice, A path independent integral and the approximate analysis of strain concentration by notches and cracks, J Appl. Mech. 35 (1968) 379–386.
[22] P.G. Bergan, C.A. Felippa, A triangular membrane element with rotational degrees of freedom, Comput. Methods Appl. Mech. Engrg. (1985).
[23] M.K. Nygård, The Free Formulation for Nonlinear Finite Elements with Applications to Shells. Div. of Structural Mechanics, Norwegian Institute of Technology, Trondheim, Norway, 1986.
[24] C. Militello, Application of parametrized variational principles to the finite element method. Ph.D Dissertation, Department of Aerospace Engineering Sciences, University of Colorado, Boulder CO, 1991.
[25] A. Hrennikoff, Solution of problems of elasticity by a framework method, J. Appl. Mech. 8 (1941) 169–175.
[26] K.C. Park, G.M. Stanley, A curved C^0 shell element based on assumed natural-coordinate strains, J. Appl. Mech. 53 (1986) 278–290.
[27] I. Fried, Orthogonal trajectory accession of the nonlinear equilibrium curve, Comput. Methods Appl. Mech. Engrg. 47 (1984) 283–298.